How to cite: *Angew. Chem. Int. Ed.* **2025**, *64*, e202415978
doi.org/10.1002/anie.202415978

Molecular Electronics

Single-Molecule Conductance of Staffanes

Ashley E. Pimentel[+], *Lan D. Pham*[+], *Veronica Carta, and Timothy A. Su**

This manuscript is dedicated to the memory of Josef Michl.

Abstract: We report the first conductance measurements of [*n*]staffane (bicyclopentane) oligomers in single-molecule junctions. Our studies reveal two quantum transport characteristics unique to staffanes that emerge from their strained bicyclic structure. First, though staffanes are composed of weakly conjugated C–C σ-bonds, staffanes carry a shallower conductance decay value ($\beta = 0.84 \pm 0.02\ n^{-1}$) than alkane chain analogs ($\beta = 0.96 \pm 0.03\ n^{-1}$) when measured with the scanning tunneling microscopy break junction (STM-BJ) technique. Staffanes are thus more conductive than other σ-bonded organic backbones reported in the literature on a per atom basis. Density functional theory (DFT) calculations suggest staffane backbones are more effective conduits for charge transport because their significant bicyclic ring strain destabilizes the HOMO-2 energy, aligning it more closely with the Fermi energy of gold electrodes as oligomer order increases. Second, the monostaffane is significantly lower conducting than expected. DFT calculations suggest that short monostaffanes sterically enforce insulating gauche interelectrode orientations over syn orientations; these steric effects are alleviated in longer staffanes. Moreover, we find that [2-5]staffane wires may accommodate axial mechanical strain by "rod-bending". These findings show for the first time how bicyclic ring strain can enhance charge transmission in saturated molecular wires. These studies showcase the STM-BJ technique as a valuable tool for uncovering the stereoelectronic proclivities of molecules at material interfaces.

Introduction

Here we report the first single-molecule conductance measurements of [*n*]staffanes and describe how bicyclic ring strain can enhance quantum transport in σ-bonded backbones. [*n*]Staffanes are polymers with bicyclo[1.1.1]pentane (staffane) repeat units.[1–4] Their rigid-rod structure led Michl and co-workers to propose their use as molecular "Tinkertoy" scaffolding in nanoarchitectures.[4–6] This rigidity has inspired the use of staffanes in molecular rotors,[7] liquid crystals,[8] donor-acceptor dyads,[9] metal–organic frameworks,[10] and next-generation therapeutics.[11–16] While the structural rigidity of staffanes is commonly emphasized, their significant bicyclic strain (65–68 kcal mol^{-1} for bicyclo[1.1.1]pentane[5]) and its influence on electronics is underappreciated. Michl and co-workers demonstrated that staffane backbones are adept at long-range spin density propagation,[17] and with Bard, showed they facilitate coupling between Ru^{2+} complexes and gold electrodes in self-assembled monolayers.[18] Others have explored the impact of staffane ring strain on molecular orbital properties in theoretical and spectroscopic studies.[19–22] Yet it has remained an open question how staffanes mediate charge transport in molecular junctions, especially compared to their commonly studied linear alkane analogs.[23] While the study of bicyclic σ-bonded wires in single-molecule junctions is gaining momentum,[24–29] it is not yet appreciated how ring strain in bicyclic systems can influence conductance. These gaps in the literature motivated us to study the length-dependent conductance properties of [*n*]staffanes **1–5** against the canonical alkane ($\mathbf{C}_n$) to understand how bicyclic ring strain and bicyclic catenation impact quantum transport.

Results and Discussion

The thiomethyl-terminated [*n*]staffanes **1–5** (Figure 1a) were prepared by the radical polymerization of [1.1.1]propellane and subsequent termination with dimethyl disulfide (Figure S1, see Supporting Information for more detail).[30–32] Each oligomer was isolated via recycling preparative gel permeation chromatography. Single-crystal X-ray diffraction (SCXRD) structures were obtained for **2**, **3**, and **4** (see Supporting Information).[33] The alkane series was synthesized as described previously.[34]

We measured the single-molecule conductance of the [*n*]staffane and alkane wires with the scanning tunneling microscopy break junction (STM-BJ) method (Figure 1c).[23]

[*] A. E. Pimentel,[+] L. D. Pham,[+] Dr. V. Carta, Prof. T. A. Su
Department of Chemistry, University of California, 92521 Riverside, California, USA
E-mail: timothys@ucr.edu
Prof. T. A. Su
Materials Science and Engineering Program, University of California, 92521 Riverside, California, USA
[+] Denotes co-first authorship

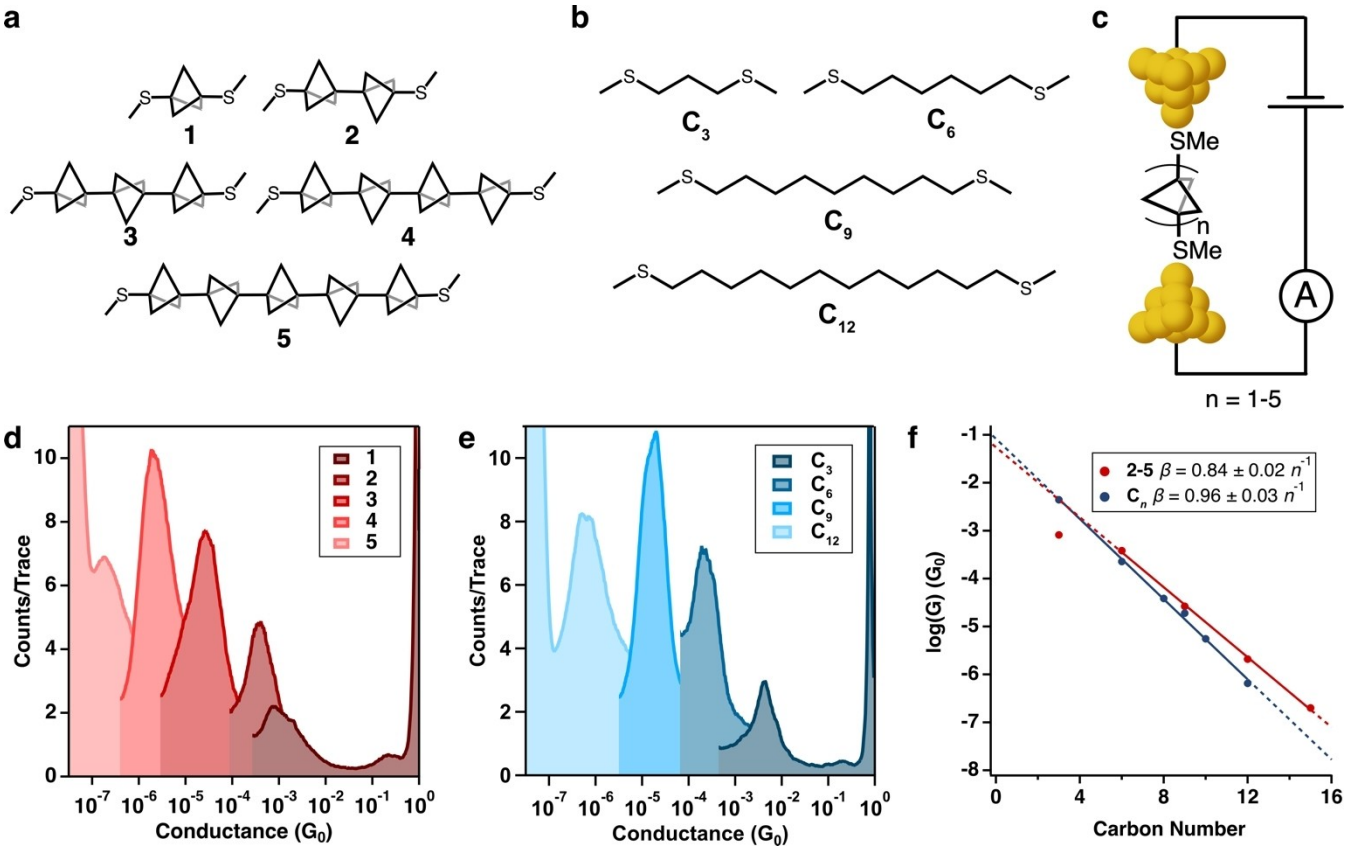

Figure 1. **(a)** Chemical structures of the measured [*n*]staffanes. **(b)** Chemical structures of measured alkanes. **(c)** Schematic of [*n*]staffane-based molecular junctions interrogated with the STM-BJ technique. **(d, e)** Overlaid 1D histograms of **1**–**5** and alkanes $\mathbf{C_3}$, $\mathbf{C_6}$, $\mathbf{C_9}$, $\mathbf{C_{12}}$. Each histogram was generated from at least 10,000 traces. All molecules were measured at gain 7. Solution concentration in 1,2,4-trichlorobenzene solvent, electrode bias, and series resistor for each molecule are as follows: **1**: 1 mM, 200 mV, 1 MΩ; **2**: 1 mM, 500 mV, 1 MΩ; **3**: 1 mM, 500 mV, 1 MΩ; **4**: 0.5 mM, 800 mV, 1 MΩ; **5**: 0.1 mM, 1500 mV, 1.47 MΩ. $\mathbf{C_3}$: 1 mM, 200 mV, 1 MΩ; $\mathbf{C_6}$: 1, mM, 345 mV, 1 MΩ; $\mathbf{C_8}$: 1 mM, 345 mV, 1 MΩ; $\mathbf{C_9}$: 1 mM, 500 mV, 1 MΩ; $\mathbf{C_{10}}$: 1 mM, 345 mV, 1 MΩ; $\mathbf{C_{12}}$: 0.1 mM, 1300 mV, 1.47 MΩ. **(f)** β-plot of staffane (red) and alkane (blue) conductance against the number of carbon atoms in the molecular backbone. Conductance values were obtained from maxima of Gaussian fits to the conductance peak in each molecule's 1D histogram.

This method is described in detail elsewhere.[35] In brief, a dilute solution (0.1–1 mM in 1,2,4-trichlorobenzene) of the molecule of interest is placed atop a substrate electrode. A gold tip electrode affixed to a motor is driven into contact with the substrate electrode, then retracted until a molecular junction is formed where the thiomethyl groups bind under-coordinated Au atoms (Figure 1c), then further retracted until the junction breaks, thus ending a single measurement trace. During this process, a voltage bias is applied between the electrodes to monitor single-molecule conductance as a function of the tip electrode displacement. Measurement parameters are listed by molecule in the caption of Figure 1. We use a high voltage bias to measure our lowest conducting molecules, **5** (1.5 V) and $\mathbf{C_{12}}$ (1.3 V), as it is required to reduce the noise floor and resolve their molecular conductance peak features; this should not influence our results too significantly, as the HOMO–LUMO gaps for these molecules are large. Thousands of single-molecule measurement traces are logarithmically binned into one-dimensional (1D) conductance histograms to relate the molecule's pickup frequency with conductance, as shown in Figure 1d, 1e, and Figure S2. Each isolated 1D histogram for the staffanes and alkanes is shown in Figure S3, S4 respectively. Two-dimensional (2D) conductance histograms relate pickup frequency to both conductance and electrode displacement (Figure S5, S6). The unit of conductance used here is the value of conductance through a single Au–Au contact, $G_0 = 2e^2/h$, where e is the charge on an electron, and h is Planck's constant.

Conductance peak width has been attributed to a number of factors, including *gauche* backbone defects,[36–41] linker-backbone coupling,[42] electrode-linker contact,[43] and electrode fluctuations.[44,45] The cage rigidity and C_3 rotational symmetry of each staffane subunit imply that the backbone geometry for staffane wires should be the same regardless of intercage rotations. In a vacuum, an invariant molecular backbone would suggest that the staffanes should have a narrow conductance distribution. Yet we find that the flexible alkanes and rigid [*n*]staffanes share similar conductance peak widths in their 1D (Figure 1d, 1e) and 2D histograms (Figure S5, S6). Figure S2b plots the 1D histograms of $\mathbf{C_9}$ and **3** to facilitate this comparison. The

conductance dispersion we observe in the [*n*]staffane histograms likely occurs from the non-equivalent dihedral rotations in the C–S bonds that connect the staffane to the electrodes, which we will explore later in this manuscript. We also find a molecular peak feature near 10^{-3} G_0 at short displacements in some alkanes (Figure S4, S6) that has also been observed in previous STM-BJ measurements of bis(thiomethyl)alkanes.[46] Its presence appears to correlate with high applied voltage bias (Figure S2c), though a full investigation on its origins is outside the scope of this manuscript.

Meanwhile, Figure 1f plots the most probable conductance peak values (Table S1) from the 1D conductance histograms of the [*n*]staffanes and alkanes. As expected for non-resonant tunneling transport, we find that conductance through the [*n*]staffanes decays exponentially with increasing oligomer length, according to the equation $G=G_c e^{-\beta L}$ where G is conductance, G_c is the contact conductance, β is the empirical beta decay value, and L is oligomer order. The β-plot comparison reveals two key differences between staffanes and alkanes: 1) staffane backbones are more effective at electronic transmission than alkane backbones, and 2) the shortest staffane **1** gives junctions with anomalously low conductance relative to the longer staffane rods. These experimental observations are rationalized below with support from density functional theory (DFT) calculations.

First, we find that for **2**–**5**, [*n*]staffane backbones ($\beta_{staffane}=0.84\pm0.02\,n^{-1}$) carry a shallower conductance decay than linear alkane backbones ($\beta_{alkane}=0.96\pm0.03\,n^{-1}$)[36–38] on a per-atom basis. To contextualize this difference, we note that **5**, which has 15 carbon atoms in its shortest linear path, is approximately as conductive as a 13-carbon alkane backbone based on β_{alkane} (Figure 1f). This is in good agreement with literature values.[38,43,46] Figure 2 shows that $\beta_{staffane}$ is demonstrably lower than those of other saturated carbon backbones beyond alkanes, including fused oligonorborane–bicyclo[2.2.0]hexane (norbornylogous) backbones ($\beta=1.0\,n^{-1}$)[47,48] and peptide backbones ($\beta=1.1\,n^{-1}$).[49–52] To our knowledge, [*n*]staffanes are the most conductive σ-bonded organic backbones reported in the literature.

At a structural level, what distinguishes staffanes from these other aliphatic backbones is their significant bicyclic cage strain, and as we will discuss below, this strain may ultimately rationalize the lower β value we find experimentally.

Frontier molecular orbital analysis via density functional theory (DFT) calculations suggests that the shallower β decay likely arises from the increasing destabilization of its HOMO-2 energy across the staffane series (Figure 3, Figure S7, Section II.a in Supporting Information). Typically, it is the highest occupied and lowest unoccupied orbitals that rationalize trend differences in electronic transmission. Yet if we compare the HOMO-1, HOMO, LUMO, and LUMO +1 of each staffane against its alkane analog, we find these energies are essentially the same (black lines, Figure 3), and are all generally within 0.1 eV, a negligible difference (Table S2). As aliphatic wires with thioether linkers have been described as HOMO-conducting molecules, we can also consider the magnitude of HOMO/HOMO-1 energy splitting as an indirect metric for the strength of coupling between the S $p\pi$ orbitals through the molecular backbone.[53]

Yet this difference in energy splitting between the alkanes and staffanes is also negligible, likely because the C–C σ-bonds in the backbone remain relatively poor conduits for interaction between the two distal S $p\pi$ pairs

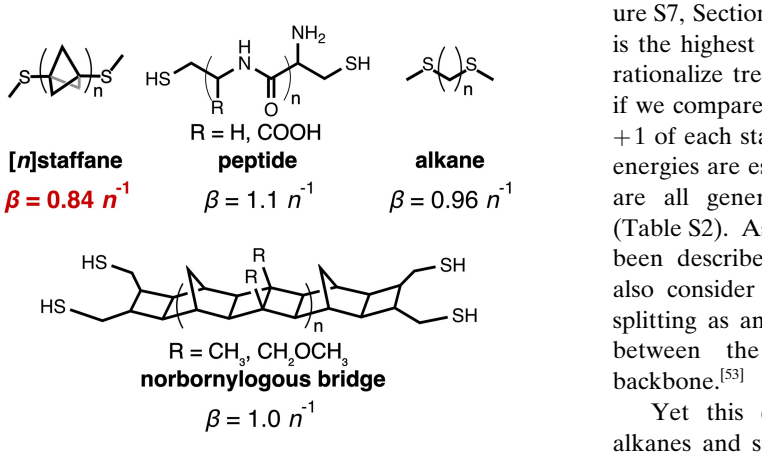

Figure 2. Chemical structures and β decay values of [*n*]staffanes **2**–**5**, peptides,[49–52] alkanes, and oligonorbornanes.[47,48] Of these C-based σ-bonded backbones, [*n*]staffanes have the lowest β decay value.

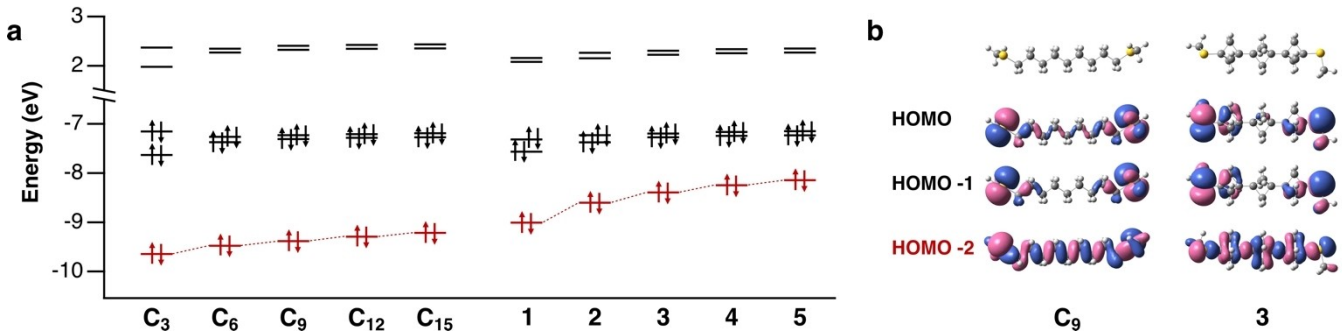

Figure 3. **(a)** Relative energies of HOMO-2 (red) to LUMO+1 levels of $\mathbf{C}_n$ alkanes and [*n*]staffanes **1**–**5**. Energy levels obtained from DFT-optimized structures at the M06-2X/6-31G** level. **(b)** MO surface plots of $\mathbf{C}_9$ and **3** (isovalue = 0.02).

both in the alkane and staffane series. These similarities point to another frontier orbital being responsible for the difference in β that we observe.

Notably, we find the HOMO-2 energies for staffanes are markedly higher than they are for alkanes: for example, the HOMO-2 energy for **3** is 1.0 eV higher than that of the analogous $\mathbf{C_9}$ alkane (Figure 3, Table S2). As the HOMO-2 in both series predominately comprises the C–C backbone σ-bonds, the heightened HOMO-2 energy for staffanes can be attributed to its strained bicyclopentane structure. Each staffane cage unit experiences: 1) significant bond angle strain (average $\theta_{CCC}=74.1°$ for **3** via SCXRD), 2) short interbridgehead distances (1.84 Å) relative to typical alkanes (2.53 Å for $\mathbf{C_3}$), and 3) significant *p*-character in its intracage C–C bonds.[54] The acute geminal interactions between high energy σ-bonds within each cage leads to higher HOMO-2 energies relative to alkanes (Figure 3b). Moreover, the HOMO-2 energy becomes far more destabilized with increasing oligomer order for staffanes. Whereas the HOMO-2 energy is 1.95 eV away from the HOMO in $\mathbf{C_{15}}$, the HOMO-2 is only 0.89 eV away from the HOMO in **5** (Figure 3a). This energetic destabilization aligns the staffane HOMO-2 more closely with the Fermi energy (E_F) as oligomer order increases, which rationalizes why staffanes are more efficient at charge transmission with increasing oligomer length compared to alkanes. It is also interesting to consider whether there are direct transport pathways between the bridgehead carbons given their short inter-bridgehead distance, though these calculations are outside the scope of the present manuscript.[17,24,54] We note the same trend occurs when a B3LYP-D3 functional is used (Figure S8).

Finally, we find the most probable conductance of the simplest staffane **1** (8.17×10^{-4} G_0, Figure 1d) is five-times lower than the β decay trendline for the longer **2**–**5** staffanes would predict (4.42×10^{-3} G_0, Figure 1f, Table S3). We note this is not a consequence of ultrashort wires, as the most probable conductance of $\mathbf{C_3}$ fits well with β_{alkane}. This suggests the trend deviation for **1** likely arises from its bicyclic structure. With support from DFT calculations, we hypothesize that the low conductance we observe arises from the preference of molecular junctions of **1** to adopt

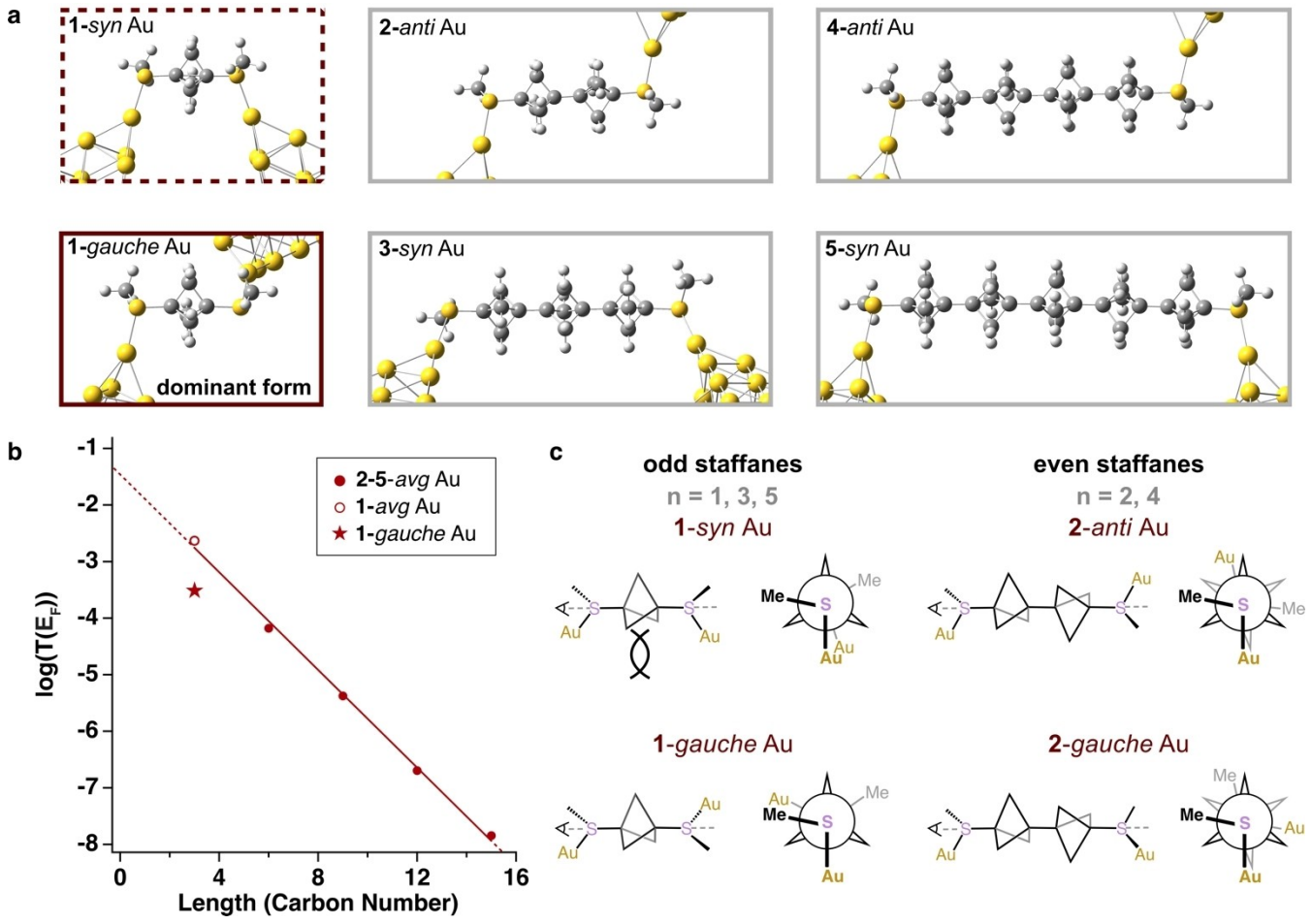

Figure 4. **(a)** Structures of [*n*]staffanes used for transmission calculations of Au_{22}-molecule-Au_{22} junctions (PBE/DZ equivalent, see Supporting Information for more details). We omit the *gauche* structures of **2**–**5** here for clarity. **(b)** 2:1 transmission at Fermi energy ($T(E_F)$) average of *gauche*:*syn*/*anti* geometries (red circles) plotted against molecular length. Transmission of gauche **1** (red star) bears greater trend resemblance to experimental data. $\beta_{1\text{–}5\text{-avg Au}}=0.99\pm0.03$ n^{-1}. **(c)** Chemical structures and Newman projections of **1** and **2** with *syn* and *gauche* Au electrode orientations. Odd-numbered staffanes adopt *syn* Au electrode orientations, whereas even-numbered staffanes adopt *anti* configurations.

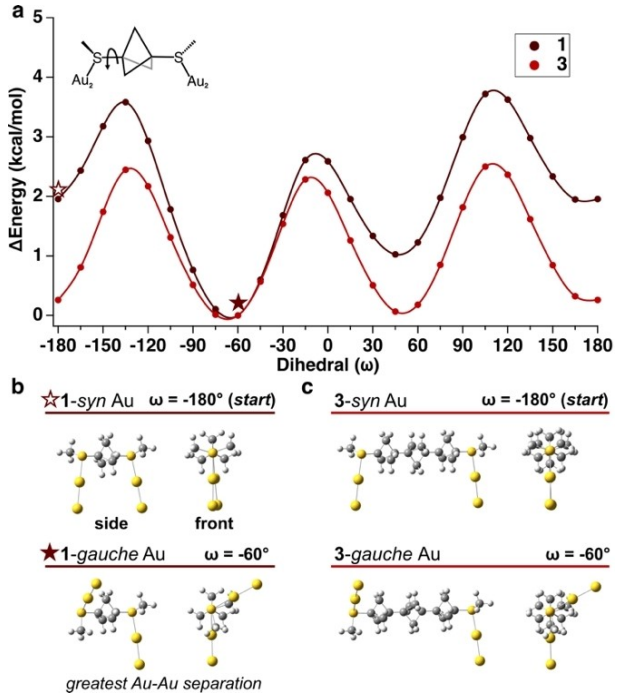

Figure 5. **(a)** DFT coordinate scans of Au–S–C–CH_2 dihedrals of **1** and **3** with Au_2 diatoms as proxies for gold electrodes (M06-2X/6-31G**(S, C, H)/def2svp(Au)). Energies are plotted relative to the energy of the lowest energy conformer for **1** or **3**. Curves are fitted with a cubic spline interpolating polynomial via Igor Pro. The *syn* electrode orientation (empty star) occurs at $\omega = -180°$. The lowest energy *gauche* orientation (filled star) occurs at $\omega = -60°$. **(b, c)** Side and front views of **(b)** Au_2-**1**-Au_2 models and **(c)** Au_2-**3**-Au_2 models from coordinate scans.

gauche-oriented instead of *syn*-oriented electrodes (Figure 4). This preference is specific to the shortest staffane **1** for two reasons: 1) there are severe steric consequences to adopting *syn*-electrode geometries across ultrashort distances in odd-numbered atomic backbones (Figure 4c), and 2) higher order staffanes can accommodate axial strain by backbone bending, whereas **1** cannot. We note that in the sections below, *syn*, *anti*, *gauche* describe the relative orientation between electrodes on each side of the molecule (Figure 4c).

We first rationalize the steric sensitivity of **1** from transmission calculations with a non-equilibrium Green's function method through the AITRANSS postprocessor module of FHI-aims (Figure 4).[55-57] Due to the C_3 symmetry of the bicyclopentane cage, each dative S–Au bond aligns with equal proclivity to any of the three C–C bonds in the attached staffane cage. If the two S–Au bonds co-align through the same *anti* C–C path through the backbone, the electrodes point in the same direction (*syn*) for odd-numbered staffanes, yet opposite directions (*anti*) for even-numbered staffanes (Figure 4a, 4c). All other endgroup dihedral combinations lead to equivalent states where their interelectrode orientation is *gauche* disposed. As the *syn* and *anti* states align through a common internal C–C *anti* path, these geometries are higher in transmission at E_F compared to their *gauche*-oriented states (Figure S9). Because *gauche* configurations are twice as probable as *anti* or *syn* geometries, we plot a 2:1 weighted average of their transmission in Figure 4b. We find that **1**–**5** fall on a common trendline if we assume that each staffane embodies this 2:1 *syn*(*anti*):*gauche* ratio. This treatment does not match our experimental data. If we instead plot the *gauche*-only transmission value for **1**, we find much better agreement with experimental trends, with the transmission of **1** falling below the **2**–**5** trendline. These transmission calculations then suggest the *syn* orientation (**1**-*syn* Au, Figure 4c) rarely occurs in molecular junctions of **1**.

Dihedral coordinate scans via DFT of **1** and **3** with Au_2 electrodes provide a qualitative understanding for why the *syn* electrode configuration is challenging to access for **1**, but not for the longer odd staffanes.[58–60] In the calculations shown in Figure 5a, we start with *syn*-disposed Au_2 electrodes, then rotate one of the Au–S–C–C dihedrals (ω) in 15° increments, optimizing geometry at each step. The minima at $\omega = \pm 180°$ represent the *syn* electrode configuration, whereas the minima at $\omega = -60°$ and $\omega = 45°$ represent *gauche* electrode configurations. For **1**, we note the *gauche* orientation at $\omega = 45°$ is energetically destabilized compared to $\omega = -60°$ because the S-methyl groups are eclipsed at this dihedral and experience steric repulsion through the short monostaffane bridge. The *gauche* state at $\omega = -60°$ (Figure 5b) is 2 kcal mol^{-1} lower in energy than the *syn* electrode state due to the steric interactions of the eclipsed Au_2 diatoms (6.2 Å Au–Au distance) through the short monostaffane bridge. We note this energy difference is likely much higher in experimental contexts, as the Au_2 electrodes in our simple model severely underapproximate the steric interactions of macroscopic electrodes.

Meanwhile for **3**, all *syn* and *gauche* configurations are essentially degenerate in energy, as the tristaffane bridge is sufficiently long to remove steric interactions between the Au_2 diatoms (12.8 Å Au–Au distance). For even-numbered staffanes, we note the *anti* and *gauche* states are similarly degenerate as is the case for **3**; the rotational scan for **2** is provided in Figure S10. Thus, **1** is unique in its preferential adoption of the less transmissive *gauche* electrode configuration due to the steric consequences of its short monostaffane bridge. We also find that in dihedral scans of the free molecule that the distal methyl groups have essentially no steric interactions between each other, even in the shortest staffane (Figure S11).

Finally, we show that when junctions of **1** do form with initial *syn* electrode orientations, they are likely pulled into *gauche* orientations to relieve the mechanical strain of junction stretching whereas longer staffanes can accommodate strain through rod-bending mechanisms. In some reports, the mechanical force applied as single-molecule junctions are measured can stretch molecules from shorter geometries into longer ones[61–63] For even-numbered staffanes, *gauche* electrode configurations are shorter than the *anti* one, while for odd-numbered staffanes, the *syn* configuration is shorter than the *gauche* ones. We thus use DFT to simulate junction stretching starting from each staffane's shortest configuration with Au_2 diatoms as proxies for electrodes (Figure 6, Figure S12).

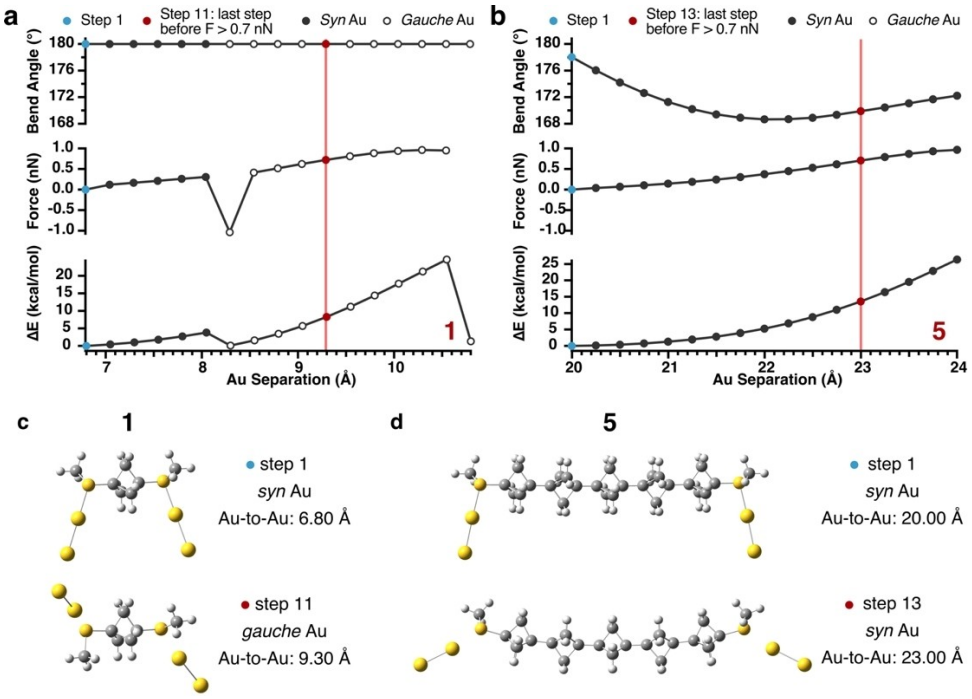

Figure 6. **(a, b)** Junction pulling calculations for **(a) 1** and **(b) 5** with Au_2 electrodes. Bend angle (top, see Figure S10), force (middle), and relative energy (bottom) plotted against the distance between Au electrodes (B3LYP-D3/6-31G**(S, C, H)/def2SVP(Au)). We note that our minimalist electrode model overapproximates the pulling force of the Au electrodes; the vertical red line thus marks a more likely 0.7 nN force threshold that has been observed to be the average breakpoint of Au-thioether dative bonds in experimental measurements. The change from filled to empty circles in **(a)** denotes a change in interelectrode geometry from *syn* to *gauche* orientations. **(c, d)** Optimized structures of **(c)** Au_2-**1**-Au_2 and Au_2-**5**-Au_2 junctions at their lowest energy optimized geometries (step 1) to their presumed junction breakpoint at 0.7 nN.

We first optimize Au_2-molecule-Au_2 geometry without constraint, then increase Au–Au separation by 0.25 Å and optimize at each Au–Au distance until a S–Au dative bond dissociates and the junction breaks. We note that the strength of the electrode-methylthiomethyl interaction is overestimated in our minimal Au_2 electrode model; experimentally, it has been shown that the average junction breaking force for dative methylthiomethyl-gold interactions is 0.7 nN.[64,65] We thus mark this 0.7 nN limit with the red lines in Figure 6 and Figure S12. These calculations were done at the B3LYP-D3/6-31G** level of theory to compare whether junction stretching in these circumstances is influenced by dispersion interactions. Our studies with the B3LYP functional without dispersion correction did not reveal any significant differences in stretching behavior (Figure S13).

Figure 6a shows that junctions of **1** that start in *syn*-oriented electrodes flip to the longer and less conductive *gauche* electrode orientations (Figure 6c) as a response to the strain imposed by increasing Au–Au distance. The longer staffanes accommodate this strain through a different mechanism. Figure 6b suggests that if **5** forms a molecular junction with *syn*-disposed electrodes in its initial state, it will maintain this *syn*-disposition even at the junction breakpoint. The longer [*n*]staffanes instead accommodate axial strain by bending the oligostaffane rod via distortion of the exocyclic C–C bonds. As more staffane units are introduced into the backbone, we find the bend angle of the staffane rod increases upon junction stretching. We define this bend as the angle C–X–C where C are distal bridgehead atoms and X is a dummy atom placed at the center of the backbone (Figure S14a). Whereas **1** does not bend at all, **5** shows the most significant deviation with a 168.7° bend.

The bending behavior of [*n*]staffanes for $n \geq 2$, but not $n = 1$, is precedented in their infrared spectroscopy studies by Michl and co-workers.[66] Connecting two staffane units together leads to the emergence of new intercage vibrational modes, including a rod-bending mode.[5] There is a relatively low barrier to this bending motion, and indeed, bent staffane rods are observed in X-ray structures from weak crystal packing influences.[67] We also observe these bends in the SCXRD structures studied here: whereas DFT-optimized structures predict 179.5° angles, we find bend angles at 176.8° (Figure S14b). In their seminal review, Michl and co-workers summarize these infrared studies with the assertion that "[*n*]staffanes resemble rubber sticks rather than steel rods"; it is this fundamental characteristic that explains why molecular junctions of **1** respond to axial force by switching from *syn* to *gauche* electrode dispositions, whereas **2** to **5** can respond by rod-bending.

Conclusion

Our comparative study of quantum transport through [*n*]staffane and alkane backbones reveal two new features of

saturated backbones that carry broader implications. First, we show how bicyclic ring strain inherent to staffanes can increase charge transmission in molecular junctions by raising the HOMO-2 energy as more staffane units are added. This strain effect may be generalizable to other molecular wires made from strained bicyclic building blocks. It is interesting to consider whether the same principles extend to other strained polyhedral oligomers such as Eaton's oligocubanes,[68,69] or whether these effects become more pronounced in heavy atom analogs such as Iwamoto's persilastaffanes[70–72] that not only experience this bicyclic strain, but are also composed of strongly delocalized Si–Si σ-bonds.

Secondly, our STM-BJ studies show that monostaffane (bicyclopentane) bridges like **1** direct the stereochemical assembly of nanoscopic objects (i.e., gold electrodes) toward *gauche* orientations. This subtle stereoelectronic distinction may similarly influence stereochemistry in the broad applications that employ bicyclopentane substructures in their molecular design, and lead us to consider how the stereochemistry of short staffane bridges may affect activity and properties in the applied areas of their use.

Acknowledgements

We thank Prof. Josef Michl for helpful discussions. This material is based upon work supported by the National Science Foundation under Grant No. CHE-2340979. Acknowledgment is made to the donors of the American Chemical Society Petroleum Research Fund for support of this research (65042-DNI7). T. A. S. acknowledges support from the Cottrell Scholars Program (CS-CSA-2024-069). Computations were performed using the computer clusters and data storage resources of the HPCC, which were funded by grants from NSF (MRI-2215705, MRI-1429826) and NIH (1S10OD016290-01 A1).

Conflict of Interest

The authors declare no conflict of interest.

Data Availability Statement

The data that support the findings of this study are available from the corresponding author upon reasonable request.

Keywords: quantum transport · single molecule electronics · staffane · molecular electronics · strain

[1] K. B. Wiberg, S. T. Waddell, K. Laidig, *Tetrahedron Lett.* **1986**, *27*, 1553–1556.
[2] A.-D. Schlüter, *Angew. Chem. Int. Ed. Engl.* **1988**, *27*, 296–298.
[3] U. Bunz, K. Polborn, H.-U. Wagner, G. Szeimies, *Chem. Ber.* **1988**, *121*, 1785–1790.
[4] Piotr. Kaszynski, Josef. Michl, *J. Am. Chem. Soc.* **1988**, *110*, 5225–5226.
[5] M. D. Levin, P. Kaszynski, J. Michl, *Chem. Rev.* **2000**, *100*, 169–234.
[6] P. Kaszynski, A. C. Friedli, J. Michl, *J. Am. Chem. Soc.* **1992**, *114*, 601–620.
[7] P. I. Dron, K. Zhao, J. Kaleta, Y. Shen, J. Wen, R. K. Shoemaker, C. T. Rogers, J. Michl, *Adv. Funct. Mater.* **2016**, *26*, 5718–5732.
[8] A. De Meijere, M. Messner, V. Vill, *Molecular Crystals and Liquid Crystals Science and Technology. Section A. Molecular Crystals and Liquid Crystals* **1994**, *257*, 161–167.
[9] A. de Meijere, L. Zhao, V. N. Belov, M. Bossi, M. Noltemeyer, S. W. Hell, *Chem. - Eur. J.* **2007**, *13*, 2503–2516.
[10] H. Yang, Y. Chen, C. Dang, A. N. Hong, P. Feng, X. Bu, *J. Am. Chem. Soc.* **2022**, *144*, 20221–20226.
[11] R. Pellicciari, M. Raimondo, M. Marinozzi, B. Natalini, G. Costantino, C. Thomsen, *J. Med. Chem.* **1996**, *39*, 2874–2876.
[12] R. Filosa, M. Carmela Fulco, M. Marinozzi, N. Giacchè, A. Macchiarulo, A. Peduto, A. Massa, P. de Caprariis, C. Thomsen, C. T. Christoffersen, R. Pellicciari, *Bioorg. Med. Chem.* **2009**, *17*, 242–250.
[13] A. F. Stepan, C. Subramanyam, I. V. Efremov, J. K. Dutra, T. J. O'Sullivan, K. J. DiRico, W. S. McDonald, A. Won, P. H. Dorff, C. E. Nolan, S. L. Becker, L. R. Pustilnik, D. R. Riddell, G. W. Kauffman, B. L. Kormos, L. Zhang, Y. Lu, S. H. Capetta, M. E. Green, K. Karki, E. Sibley, K. P. Atchison, A. J. Hallgren, C. E. Oborski, A. E. Robshaw, B. Sneed, C. J. O'Donnell, *J. Med. Chem.* **2012**, *55*, 3414–3424.
[14] R. Gianatassio, J. M. Lopchuk, J. Wang, C.-M. Pan, L. R. Malins, L. Prieto, T. A. Brandt, M. R. Collins, G. M. Gallego, N. W. Sach, J. E. Spangler, H. Zhu, J. Zhu, P. S. Baran, *Science* **2016**, *351*, 241–246.
[15] F. Lovering, J. Bikker, C. Humblet, *J. Med. Chem.* **2009**, *52*, 6752–6756.
[16] B. R. Shire, E. A. Anderson, *JACS Au* **2023**, *3*, 1539–1553.
[17] A. J. McKinley, P. N. Ibrahim, V. Balaji, J. Michl, *J. Am. Chem. Soc.* **1992**, *114*, 10631–10637.
[18] Y. S. Obeng, M. E. Laing, A. C. Friedli, H. C. Yang, D. Wang, E. W. Thulstrup, A. J. Bard, J. Michl, *J. Am. Chem. Soc.* **1992**, *114*, 9943–9952.
[19] M. Braga, *Chem. Phys.* **1996**, *213*, 159–164.
[20] M. J. Shephard, M. N. Paddon-Row, K. D. Jordan, *Chem. Phys.* **1993**, *176*, 289–304.
[21] M. N. Paddon-Row, K. D. Jordan, *J. Am. Chem. Soc.* **1993**, *115*, 2952–2960.
[22] R. Gleiter, K.-H. Pfeifer, G. Szeimies, U. Bunz, *Angew. Chem. Int. Ed. Engl.* **1990**, *29*, 413–415.
[23] B. Xu, N. J. Tao, *Science* **2003**, *301*, 1221–1223.
[24] M. H. Garner, H. Li, Y. Chen, T. A. Su, Z. Shangguan, D. W. Paley, T. Liu, F. Ng, H. Li, S. Xiao, C. Nuckolls, L. Venkataraman, G. C. Solomon, *Nature* **2018**, *558*, 416–419.
[25] M. H. Garner, M. Koerstz, J. H. Jensen, G. C. Solomon, *J. Phys. Chem. Lett.* **2018**, *9*, 6941–6947.
[26] M. H. Garner, H. Li, M. Neupane, Q. Zou, T. Liu, T. A. Su, Z. Shangguan, D. W. Paley, F. Ng, S. Xiao, C. Nuckolls, L. Venkataraman, G. C. Solomon, *J. Am. Chem. Soc.* **2019**, *141*, 15471–15476.
[27] M. H. Garner, M. Koerstz, J. H. Jensen, G. C. Solomon, *ACS Phys. Chem Au* **2022**, *2*, 282–288.
[28] H. Li, M. H. Garner, Z. Shangguan, Y. Chen, Q. Zheng, T. A. Su, M. Neupane, T. Liu, M. L. Steigerwald, F. Ng, C. Nuckolls, S. Xiao, G. C. Solomon, L. Venkataraman, *J. Am. Chem. Soc.* **2018**, *140*, 15080–15088.
[29] B. Zhang, M. H. Garner, L. Li, L. M. Campos, G. C. Solomon, L. Venkataraman, *Chem. Sci.* **2021**, *12*, 10299–10305.

[30] R. M. Bär, L. Langer, M. Nieger, S. Bräse, *Adv. Synth. Catal.* **2020**, *362*, 1356–1361.
[31] U. Bunz, K. Polborn, H. Wagner, G. Szeimies, *Chem. Ber.* **1988**, *121*, 1785–1790.
[32] R. Gianatassio, J. M. Lopchuk, J. Wang, C.-M. Pan, L. R. Malins, L. Prieto, T. A. Brandt, M. R. Collins, G. M. Gallego, N. W. Sach, J. E. Spangler, H. Zhu, J. Zhu, P. S. Baran, *Science* **2016**, *351*, 241–246.
[33] *Deposition numbers 2377792 (for 2), 2377794 (for 3), and 2377793 (for 4) contain the supplementary crystallographic data for this paper. These data are provided free of charge by the Joint Cambridge Crystallographic Data Centre and Fachinformationszentrum Karlsruhe Access Structures Service.*
[34] H. Li, M. H. Garner, T. A. Su, A. Jensen, M. S. Inkpen, M. L. Steigerwald, L. Venkataraman, G. C. Solomon, C. Nuckolls, *J. Am. Chem. Soc.* **2017**, *139*, 10212–10215.
[35] T. A. Su, M. Neupane, M. L. Steigerwald, L. Venkataraman, C. Nuckolls, *Nat. Rev. Mater.* **2016**, *1*, 1–15.
[36] W. Haiss, H. van Zalinge, D. Bethell, J. Ulstrup, D. J. Schiffrin, R. J. Nichols, *Faraday Discuss.* **2006**, *131*, 253–264.
[37] D. R. Jones, A. Troisi, *J. Phys. Chem. C* **2007**, *111*, 14567–14573.
[38] C. Li, I. Pobelov, T. Wandlowski, A. Bagrets, A. Arnold, F. Evers, *J. Am. Chem. Soc.* **2008**, *130*, 318–326.
[39] L. Mejía, N. Renaud, I. Franco, *J. Phys. Chem. Lett.* **2018**, *9*, 745–750.
[40] Z. Li, L. Mejía, J. Marrs, H. Jeong, J. Hihath, I. Franco, *J. Phys. Chem. C* **2021**, DOI 10.1021/acs.jpcc.0c08428.
[41] S. Martín, F. Giustiniano, W. Haiss, S. J. Higgins, R. J. Whitby, R. J. Nichols, *J. Phys. Chem. C* **2009**, *113*, 18884–18890.
[42] Y. S. Park, J. R. Widawsky, M. Kamenetska, M. L. Steigerwald, M. S. Hybertsen, C. Nuckolls, L. Venkataraman, *J. Am. Chem. Soc.* **2009**, *131*, 10820–1.
[43] F. H. Van Veen, L. Ornago, H. S. J. Van Der Zant, M. El Abbassi, *J. Phys. Chem. C* **2022**, *126*, 8801–8806.
[44] W. Haiss, S. Martín, E. Leary, H. V. Zalinge, S. J. Higgins, L. Bouffier, R. J. Nichols, *J. Phys. Chem. C* **2009**, *113*, 5823–5833.
[45] O. Adak, E. Rosenthal, J. Meisner, E. F. Andrade, A. N. Pasupathy, C. Nuckolls, M. S. Hybertsen, L. Venkataraman, *Nano Lett.* **2015**, *15*, 4143–4149.
[46] M. S. Inkpen, Z. Liu, H. Li, L. M. Campos, J. B. Neaton, L. Venkataraman, *Nat. Chem.* **2019**, *11*, 351–358.
[47] W. R. Yang, M. W. Jones, X. Li, P. K. Eggers, N. Tao, J. J. Gooding, M. N. Paddon-Row, *J. Phys. Chem. C* **2008**, *112*, 9072–9080.
[48] N. Darwish, M. N. Paddon-Row, J. J. Gooding, *Acc. Chem. Res.* **2014**, *47*, 385–395.
[49] X. Xiao, B. Xu, N. Tao, *J. Am. Chem. Soc.* **2004**, *126*, 5370–5371.
[50] M. M. Thuo, W. F. Reus, F. C. Simeone, C. Kim, M. D. Schulz, H. J. Yoon, G. M. Whitesides, *J. Am. Chem. Soc.* **2012**, *134*, 10876–10884.
[51] J. M. Brisendine, S. Refaely-Abramson, Z.-F. Liu, J. Cui, F. Ng, J. B. Neaton, R. L. Koder, L. Venkataraman, *J. Phys. Chem. Lett.* **2018**, *9*, 763–767.
[52] J. Juhaniewicz, J. Pawlowski, S. Sek, *Isr. J. Chem.* **2015**, *55*, 645–660.
[53] T. A. Su, M. Neupane, M. L. Steigerwald, L. Venkataraman, C. Nuckolls, *Nat. Rev. Mater.* **2016**, *1*, 16002.
[54] G. C. Solomon, C. Herrmann, T. Hansen, V. Mujica, M. A. Ratner, *Nat. Chem.* **2010**, *2*, 223–8.
[55] V. Blum, R. Gehrke, F. Hanke, P. Havu, V. Havu, X. Ren, K. Reuter, M. Scheffler, *Comput. Phys. Commun.* **2009**, *180*, 2175–2196.
[56] A. Arnold, F. Weigend, F. Evers, *J. Chem. Phys.* **2007**, *126*, 174101.
[57] A. Bagrets, *J. Chem. Theory Comput.* **2013**, *9*, 2801–2815.
[58] We note that Au_2 electrodes severely underapproximate the steric effects of macroscale electrodes, but are sufficient to provide a qualitative understanding of how molecular junction geometry relates to observed conductance data.
[59] M. O. Hight, J. Y. Wong, A. E. Pimentel, T. A. Su, *J. Am. Chem. Soc.* **2024**, *146*, 4716–4726.
[60] S. T. Schneebeli, M. Kamenetska, Z. Cheng, R. Skouta, R. A. Friesner, L. Venkataraman, R. Breslow, *J. Am. Chem. Soc.* **2011**, *133*, 2136–9.
[61] T. A. Su, H. Li, M. L. Steigerwald, L. Venkataraman, C. Nuckolls, *Nature Chem* **2015**, *7*, 215–220.
[62] I. Franco, G. C. Solomon, G. C. Schatz, M. A. Ratner, *J. Am. Chem. Soc.* **2011**, *133*, 15714–15720.
[63] S. Y. Quek, M. Kamenetska, M. L. Steigerwald, H. J. Choi, S. G. Louie, M. S. Hybertsen, J. B. Neaton, L. Venkataraman, *Nature Nanotech* **2009**, *4*, 230–234.
[64] M. Frei, S. V. Aradhya, M. S. Hybertsen, L. Venkataraman, *J. Am. Chem. Soc.* **2012**, *134*, 4003–4006.
[65] S. V. Aradhya, J. S. Meisner, M. Krikorian, S. Ahn, R. Parameswaran, M. L. Steigerwald, C. Nuckolls, L. Venkataraman, *Nano Lett.* **2012**, *12*, 1643–1647.
[66] M. S. Gudipati, S. J. Hamrock, V. Balaji, J. Michl, *J. Phys. Chem.* **1992**, *96*, 10165–10176.
[67] A. C. Friedli, V. M. Lynch, P. Kaszynski, J. Michl, *Acta Crystallogr. Sect. B* **1990**, *46*, 377–389.
[68] P. E. Eaton, Michele. Maggini, *J. Am. Chem. Soc.* **1988**, *110*, 7230–7232.
[69] P. E. Eaton, *Angew. Chem. Int. Ed. Engl.* **1992**, *31*, 1421–1436.
[70] T. Iwamoto, D. Tsushima, E. Kwon, S. Ishida, H. Isobe, *Angew. Chem. Int. Ed.* **2012**, *51*, 2340–2344.
[71] Y. Yokouchi, T. Iwamoto, *Organometallics* **2020**, *39*, 3301–3305.
[72] Y. Morino, S. Ishida, T. Iwamoto, *Z. Anorg. Allg. Chem.* **2024**, *650*, e202400056.

Manuscript received: August 20, 2024
Accepted manuscript online: September 30, 2024
Version of record online: November 6, 2024